Characterization of Mobile Ions in Perovskite Solar Cells with Capacitance and Current Measurements by Approximating Drift-Diffusion Simulations

Moritz C. Schmidt,[1] Agustin O. Alvarez,[1] Biruk A. Seid,[2] Jeroen J. de Boer,[1] Felix Lang,[2] and Bruno Ehrler[1,*]

[1] *LMPV—Sustainable Energy Materials Department, AMOLF, Science Park 104, 1098 XG Amsterdam, Netherlands*

[2] *ROSI Freigeist Juniorgroup, Institut für Physik und Astronomie, University of Potsdam, Karl-Liebknecht-Str. 24/25, 14476 Potsdam-Golm, Germany*

(Received 17 May 2025; revised 23 July 2025; accepted 12 August 2025; published 16 September 2025)

The migration of mobile ions is one of the leading causes of the degradation of perovskite solar cells. However, quantifying mobile ions in complete perovskite solar cells is challenging due to the complex device stacks and the impact of charge transport layers on the measurement techniques. Here we develop a simple and openly accessible *step model* that approximates drift-diffusion simulations. The step model is based on the expression of the charge density in the ionic and electronic accumulation and depletion layers as step functions. We can then accurately determine the impact of mobile ions on the dc potential distribution of perovskite solar cells. Furthermore, we can simulate electrical measurement techniques commonly used to quantify mobile ions: capacitance transient, current transient, and capacitance-frequency measurements. By validating the step model with drift-diffusion simulations, we show that an accurate extraction of ion density, diffusion coefficient, and activation energy is possible in an accessible range. We finally apply the step model developed to estimate the ionic conductivity and activation energy of perovskite solar cells.

DOI: 10.1103/mr3l-jg9h

I. INTRODUCTION

The efficiency of single-junction perovskite solar cells reached 27.0 % in 2024, directly competing with silicon-based solar cells, with an efficiency of 27.3 % [1,2]. Also, the longevity of perovskite solar cells has significantly increased in recent years, with operational stability now reaching thousands of hours [3,4]. This value, however, is still not enough and hinders the commercialization of perovskite-based solar cells. Stability issues are often related to mobile ions in the perovskite. These can migrate into the charge transport layers (CTLs), introducing traps and decreasing the conductivity [5]. Ion-induced phase segregation in mixed-halide perovskites has been linked to open-circuit voltage losses [6,7]. Additionally, mobile ions can significantly alter the potential distribution of perovskite solar cells by screening the built-in voltage, which can lead to significant short-circuit current losses. This change in current leads to hysteresis in J-V measurements if the scan speed matches the timescale of ion migration [8–10]. To better understand the impact of mobile ions on the stability of perovskite solar cells, an accurate characterization of the ionic conductivity and the ion density is important. Electrical measurements are becoming increasingly popular to quantify mobile ions due to their ease of use and nondestructive nature. These techniques include transient current measurements (also known as bias-assisted charge extraction) [9,11–13], impedance and capacitance spectroscopy [14–16], and measurements of capacitance transients (also known as transient ion drift) [17,18]. However, interpretation of the results is difficult, as transport layers can significantly impact electrical measurements [19,20]. One prominent example is capacitance transient measurements. Contrary to our initially proposed interpretation [18], we later showed that most of the dynamics in this measurement technique occur due to a modulation of the transport layer capacitances [21]. One option to circumvent the impact of transport layers on electrical measurements is to focus on the characterization of transport-layer-free devices [13,14,16]. Another option is to account for the impact of transport layers by the use of drift-diffusion simulations, a common tool to understand the device physics of perovskite solar cells [22–25]. However, drift-diffusion simulations can be computationally intensive, which makes screening large ranges of device parameters difficult. A compromise between accuracy and simplicity is to approximate drift-diffusion simulations

*Contact author: b.ehrler@amolf.nl

with a model that is computationally less intensive and still describes the device reasonably accurately. One example is the surface polarization model developed by Courtier *et al.* [26,27], which is based on an accurate, yet still complex approximation of the Debye accumulation layers. Bertoluzzi *et al.* [28] developed an elegant approximation of the potential distribution in the perovskite by approximating the net charge density of the ionic accumulation and depletion layers as step functions and estimated mobile ion densities on the basis of current transient measurements. However, their model did not account for potential drops in the transport layers and allowed only the approximation of current transients.

Here we extend the model proposed by Bertoluzzi *et al.* [28] to approximate current transient, capacitance transient, and capacitance-frequency measurements of complete devices in the dark. The time-dependent measurements chosen can easily be applied to characterize ionic processes in the second-to-hour range. Capacitance-frequency measurements are especially suitable for ionic processes in the millisecond-to-second range. Therefore, the techniques chosen cover all timescales on which ion migration occurs. Furthermore, combining the different techniques is a powerful way to cross-validate the results [16]. The model is based on approximation of the net charge density in the ionic accumulation and depletion layers in the perovskite and the depletion layers in the CTLs with step functions. This description allows an accurate approximation of the potential through perovskite solar cells. We further extend the model by computing the time-dependent charge and potential distributions depending on the ionic conductivity of the perovskite, resulting in an approximation of current transient measurements. Additionally, we solve the small-signal solution, allowing us to compute capacitance transient measurements and capacitance-frequency measurements at 0 V dc bias. Hereafter, we refer to the approximation as the "step model." By benchmarking the step model with drift-diffusion simulations using the simulation software SETFOS [29], we demonstrate that we can accurately determine the ionic conductivity and, in a range, also the ion density of perovskite solar cells. Lastly, we experimentally determine the ionic conductivity of triple cation perovskite solar cells by fitting the step model to capacitance transient, current transient, and capacitance-frequency measurements.

In combination with the simplicity of the measurements, the model developed here offers a powerful tool to quantify mobile ions in perovskite solar cells and is openly accessible [30].

II. RESULTS AND DISCUSSION

To derive a model for the capacitance transient, current transient, and capacitance-frequency measurements, we first have to make some assumptions about the perovskite solar cell. Similarly to other studies [28,31,32], we assume that halide vacancies V_X^+ are the dominant migrating species due to their lower activation energy, which has been theoretically predicted [33–35]. We further assume that these mobile halide vacancies are compensated by immobile anion vacancies V_A^- [36] or halide interstitial ions X_i^- [37], leading to overall charge neutrality in the perovskite. Because all measurements are done in the dark and at 0 V dc bias, the electric carrier density in the perovskite and the minority carrier density at the perovskite/CTL interfaces are low. Thus, recombination in the bulk and at the interfaces will not significantly impact the measurements. Therefore, we do not include recombination processes in the model. We additionally assume that defect doping is negligible, which has been shown for well-performing lead-based perovskite solar cells [38]. Consequently, we assume that the mobile ionic carriers dominate the potential profile in the perovskite. The impact of mobile halide vacancies on the potential of a device is illustrated in Fig. 1. In Fig. 1(a), positively charged mobile halide vacancies are distributed homogeneously throughout the perovskite. In this case, because the net charge density in the perovskite is zero (due to compensation by negative ions), the potential drops linearly within the perovskite. We refer to this case as "no screening." In the second case, in Fig. 1(b), the halide vacancies accumulate at the hole transport layer (HTL)/perovskite interface, screening the built-in voltage of the device. The accumulation of halide vacancies comes with a simultaneous depletion of halide vacancies at the perovskite/electron transport layer (ETL) interface and a depletion of electronic carriers in the CTLs [21]. Altogether, the potential drops mainly in the CTLs and the ionic accumulation and depletion layers. We refer to this case as "screening." In equilibrium at 0 V applied bias, the device is in the *screening* case. When a voltage pulse is applied to the device, like in current transient or capacitance transient measurements, as illustrated in Fig. 1(c), mobile ions diffuse away from the interface. Then, after removal of the applied bias, the device potential is similar to that in the *no screening* case. With increasing time, more and more ions drift to the HTL/perovskite interface, ultimately resulting in the *screening* case. In capacitance-frequency measurements at 0 V, the device is in the *screening* case. At high frequencies, the geometrical capacitance C_{geo} of the device is probed, as illustrated in Fig. 1(c). At low frequencies, the capacitance increases due to ionic polarization [20,39].

To illustrate the step model, we compare it with drift-diffusion simulations of a semiconductor stack resembling a perovskite solar cell. The device stack is illustrated in Fig. 1(a), and the simulation parameters are listed in Table S1 in Supplemental Material [40]. For illustration purposes, we use a slightly doped HTL and a slightly doped ETL, $N_{\mathrm{D,ETL}} = N_{\mathrm{A,HTL}} = 5 \times 10^{17}\,\mathrm{cm}^{-3}$,

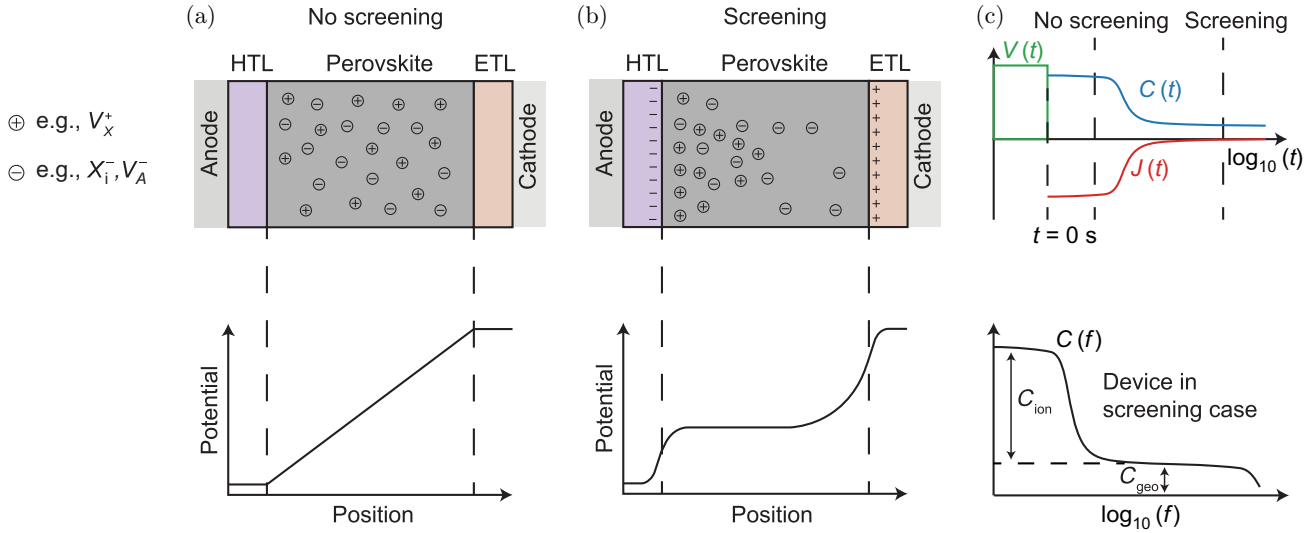

FIG. 1. Impact of mobile ions on the potential in a perovskite solar cell. In the *no screening* case in (a), the mobile ions are distributed homogeneously, and the potential drops linearly across the perovskite. In the *screening* case in (b), the mobile ions accumulate at the HTL/perovskite interface, screening the built-in voltage of the device, resulting in a flat potential in the perovskite bulk. (c) Capacitance transient $C(t)$ and current transient $J(t)$ after a voltage pulse $V(t)$ and capacitance-frequency $C(f)$ techniques.

with different dielectric constants ($\epsilon_{r,HTL} = 4$ and $\epsilon_{r,ETL} = 8$). First, we focus on approximating the DC solution of the potential and net charge density, which will enable the calculation of current transients. Then, we focus on applying the sinusoidal steady state analysis [41] to approximate capacitance transient and capacitance-frequency measurements.

A. Approximation of the dc solution

Our first focus is to approximate the dc potential profile within the perovskite solar cell, which is dominated by mobile ions. Bertoluzzi *et al.* [28] showed that approximating the charge density of the ionic accumulation and depletion layers within the perovskite with step functions leads to good agreement with drift-diffusion simulations. However, their model accounted only for the approximation of the potential in the perovskite layer (not taking CTLs into account). Therefore, we extend the step function approximation and apply it to the depletion layers in the CTLs. Figures 2(a) and 2(b) illustrate the approximation of the net charge densities for the earlier described *no screening* and *screening* cases. We divide the device into five regions, shown in Figs. 2(a) and 2(b). At the interfaces between the perovskite and the CTLs, we define the ionic accumulation layer and the ionic depletion layer in the perovskite (regions II and IV). Their net charge densities and widths are en_{II} and w_{II}, and en_{IV} and w_{IV}, respectively. In the perovskite bulk, the net charge density en_{III} is zero, as the mobile ions and the immobile ions compensate each other. The accumulation of mobile ions at the HTL/perovskite interface leads to a depletion of holes from the HTL (region I). We define the charge density and width of this depletion layer as en_I and w_I. Similarly, the depletion of mobile ions at the perovskite/ETL interface leads to a depletion of electrons from the ETL (region V), which we describe with the charge density en_V and width w_V. With this, we can summarize the net charge density in the device as follows:

$$\rho(x) = \begin{cases} -en_I & \text{in region I (depletion layer in the HTL),} \\ en_{II} & \text{in region II (ionic accumulation layer in the perovskite),} \\ 0 & \text{in region III (perovskite bulk),} \\ -en_{IV} & \text{in region IV (ionic depletion layer in the perovskite),} \\ en_V & \text{in region V (depletion layer in the ETL),} \\ 0 & \text{otherwise,} \end{cases} \tag{1}$$

where e is the elementary charge. We can calculate the position-dependent one-dimensional electric field $E(x)$ through the device with Gauss's law [42]

$$\frac{dE(x)}{dx} = \frac{\rho(x)}{\epsilon} \tag{2}$$

and the potential profile $\Phi(x)$ through the device with

$$\frac{d\Phi(x)}{dx} = -E(x). \tag{3}$$

A detailed derivation of the electric field and potential is given in Supplemental Material [40]. Ultimately, we arrive at an expression for the individual potential drops within the different regions:

$$\Delta\Phi = \begin{cases} \frac{en_{\mathrm{I}}w_{\mathrm{I}}^2}{2\epsilon_0\epsilon_{\mathrm{r,HTL}}} & \text{in region I (depletion layer in the HTL),} \\ \frac{en_{\mathrm{II}}w_{\mathrm{II}}^2}{2\epsilon_0\epsilon_{\mathrm{r,pero}}} - E_{\mathrm{bulk}}w_{\mathrm{II}} & \text{in region II (ionic accumulation layer in the perovskite),} \\ -E_{\mathrm{bulk}}(d_{\mathrm{pero}} - w_{\mathrm{II}} - w_{\mathrm{IV}}) & \text{in region III (perovskite bulk),} \\ \frac{en_{\mathrm{IV}}w_{\mathrm{IV}}^2}{2\epsilon_0\epsilon_{\mathrm{r,pero}}} - E_{\mathrm{bulk}}w_{\mathrm{IV}} & \text{in region IV (ionic depletion layer in the perovskite),} \\ \frac{en_{\mathrm{V}}w_{\mathrm{V}}^2}{2\epsilon_0\epsilon_{\mathrm{r,ETL}}} & \text{in region V (depletion layer in the ETL),} \end{cases} \tag{4}$$

where E_{bulk} is the electric field in region III, ϵ_0 is the vacuum permittivity, and $\epsilon_{\mathrm{r,HTL}}$, $\epsilon_{\mathrm{r,pero}}$, and $\epsilon_{\mathrm{r,ETL}}$ are the relative permittivities in the different layers. The overall sum of these potential drops has to equal the potential difference at the electrodes, which is dependent on the built-in potential V_{BI} and the externally applied bias V_{app} [27]:

$$V_{\mathrm{BI}} - V_{\mathrm{app}} = \Delta\Phi_{\mathrm{I}} + \Delta\Phi_{\mathrm{II}} + \Delta\Phi_{\mathrm{III}} + \Delta\Phi_{\mathrm{IV}} + \Delta\Phi_{\mathrm{V}} \tag{5}$$

$$= \frac{e}{2\epsilon_0}\left(\frac{n_{\mathrm{I}}w_{\mathrm{I}}^2}{\epsilon_{\mathrm{r,HTL}}} + \frac{n_{\mathrm{II}}w_{\mathrm{II}}^2}{\epsilon_{\mathrm{r,pero}}} + \frac{n_{\mathrm{IV}}w_{\mathrm{IV}}^2}{\epsilon_{\mathrm{r,pero}}} + \frac{n_{\mathrm{V}}w_{\mathrm{V}}^2}{\epsilon_{\mathrm{r,ETL}}}\right) - E_{\mathrm{bulk}}d_{\mathrm{pero}}. \tag{6}$$

Some of the densities and widths are readily accessible from the device parameters. For example, the carrier density in the ionic depletion region n_{IV} can be approximated with the density of immobile negative ions, which is simply the ion density N_{ion}. Furthermore, the carrier densities in the depletion layers are the doping densities of the transport layers $N_{\mathrm{A,HTL}}$ and $N_{\mathrm{D,ETL}}$. Additionally, the total charge in the ionic accumulation layer and the ionic depletion layer has to be equal ($en_{\mathrm{II}}w_{\mathrm{II}} = en_{\mathrm{IV}}w_{\mathrm{IV}}$). Assuming there is no polarization at the interfaces, the electric displacement field throughout the device and, importantly, at the interfaces, must be constant, resulting in expressions for the depletion and accumulation widths in the transport layers as a function of n_{II}. Lastly, we can approximate the width of the ionic accumulation layer with the Debye length [28]:

$$L_{\mathrm{D}} = \sqrt{\frac{\epsilon_0\epsilon_{\mathrm{r,pero}}k_{\mathrm{B}}T}{e^2N_{\mathrm{ion}}}}, \tag{7}$$

where k_{B} is the Boltzmann constant and T is the temperature. With these constraints and simplifications, we finally arrive at an expression for the bulk electric field E_{bulk} that depends only on the density of accumulated ions at the HTL/perovskite interface (see Sec. S1 A in Supplemental Material [40] for the complete derivation).

Next, we introduce time dependence into the step model. The starting point is the *no screening* case depicted in Figs. 2(a) and 2(c), which illustrate the charge densities and potential after application of a voltage pulse. In this case, the density of accumulated ions at the HTL/perovskite interface is low [see Fig. 2(a)], leading to a large potential drop in the perovskite bulk [see Fig. 2(c)], and consequently a large bulk electric field E_{bulk}. This electric field drives mobile ions to the HTL/perovskite interface when the voltage pulse is removed. We can, therefore, express the time-dependent change of accumulated ions at the interface as [32,43]

$$\frac{dn_{\mathrm{II}}(t)}{dt} = -\frac{1}{ew_{\mathrm{II}}}\underbrace{eN_{\mathrm{ion}}\mu_{\mathrm{ion}}E_{\mathrm{bulk}}(t)}_{J_{\mathrm{ion}}(t)} \tag{8}$$

$$= -\frac{1}{w_{\mathrm{II}}k_{\mathrm{B}}T}eN_{\mathrm{ion}}D_{\mathrm{ion}}E_{\mathrm{bulk}}(t), \tag{9}$$

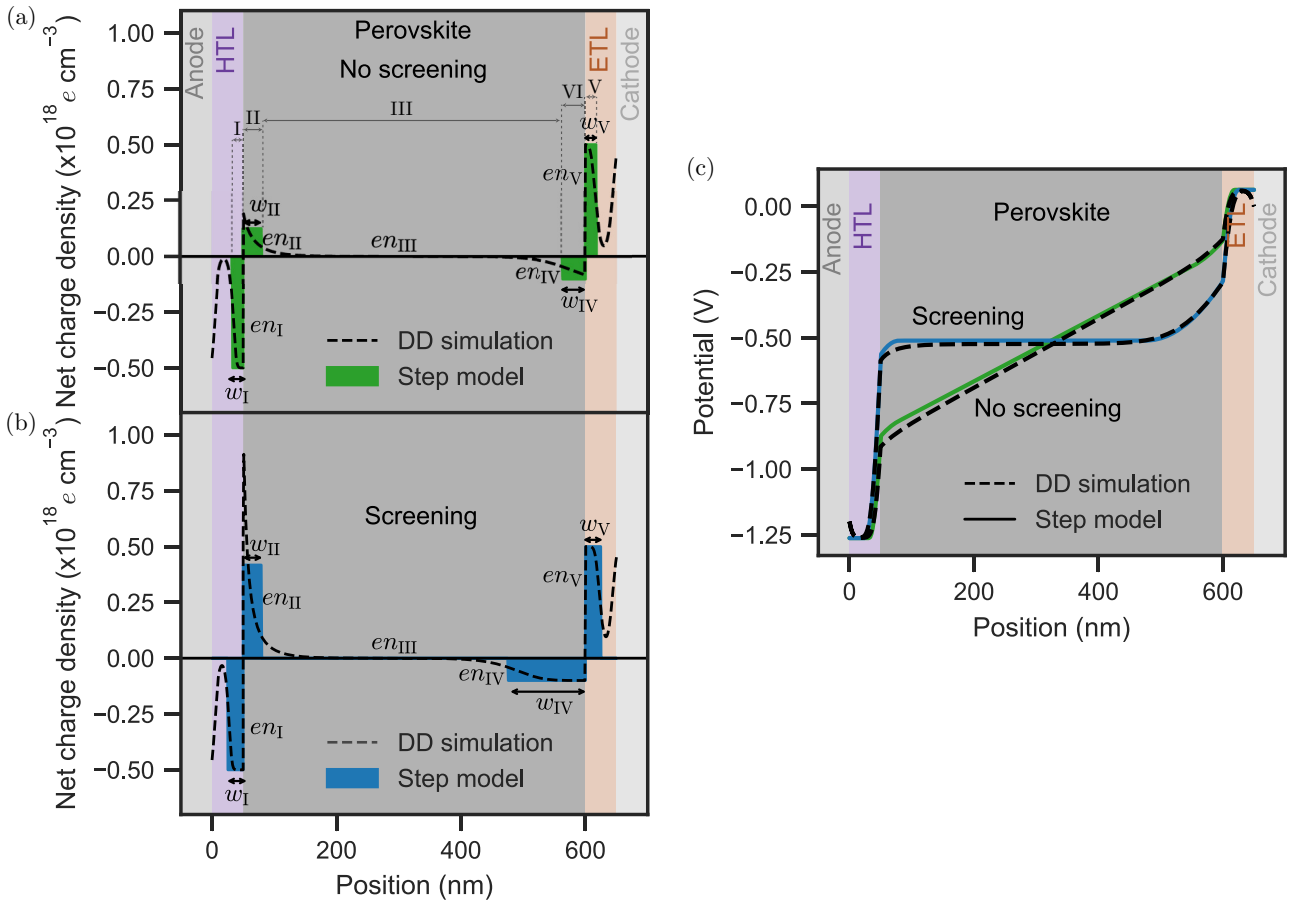

FIG. 2. Comparison of the net charge density simulated with drift-diffusion (DD) simulations and the step model for (a) the *no screening* case and (b) the *screening* case. (c) Comparison of the potentials simulated with the step model and drift-diffusion simulations.

where μ_{ion} is the mobility and D_{ion} is the diffusion coefficient of mobile ions. This is an ordinary differential equation, as the electric field $E_{\text{bulk}}(t)$ depends on the density of accumulated ions $n_{\text{II}}(t)$ [see Eq. (S41) in Supplemental Material [40]]. After the applied bias is removed, more and more mobile ions accumulate at the HTL/perovskite interface. Simultaneously, the potential drop in all depletion and accumulation layers increase, resulting in a smaller bulk electric field and, consequently, a smaller ionic current. Finally, when enough mobile ions accumulate at the HTL/perovskite interface, the built-in potential is screened, and no more ions will accumulate at the interface, resulting in the *screening* case in Fig. 2(b) and the corresponding potential in Fig. 2(c). We can solve the differential equation numerically. The result is a time-dependent density of accumulated ions at the HTL/perovskite interface $n_{\text{II}}(t)$. With $n_{\text{II}}(t)$, we can calculate the time-dependent net charge densities in all other regions and approximate the time-dependent potential within the device. Figures 2(a) and 2(b) show good agreement between the approximated net charge densities and drift-diffusion simulations. The approximated potential distributions within the device for both the *no screening* case and the *screening* case also agree well with the drift-diffusion simulations, as shown in Fig. 2(c).

When the applied bias is high enough, mobile ions can accumulate at the opposite perovskite/ETL interface. Then, the ionic depletion layer is at the HTL/perovskite interface, whereas the ionic accumulation layer is at the perovskite/ETL interface, which is illustrated in Fig. S5(a) in Supplemental Material [40]. At even higher voltages, electronic carriers will screen the accumulated ions at the perovskite/CTL interfaces [see Fig. S5(b)]. Importantly, the step model can also approximate the potential in undoped CTLs as shown in Fig. S6 in Supplemental Material [40]. Interface effects, such as polarization, are currently not accounted for by the step model. Additionally, doping in the perovskite layer is not included in the step model, but could significantly impact the potential distribution, for example, in tin-based perovskites [44].

With the dc solution of the potential, we can compute the current transient after application of a voltage pulse. In the center of the perovskite, the current density depends on the ionic current and the displacement current due to the

change in the electric field. Because the current density is constant throughout the device, we can define the extracted current as

$$J_{\mathrm{dc}}(t) = eN_{\mathrm{ion}}\mu_{\mathrm{ion}}E_{\mathrm{bulk}}(t) + \epsilon_0\epsilon_{\mathrm{r,pero}}\frac{dE_{\mathrm{bulk}}(t)}{dt}. \tag{10}$$

A comparison of the approximated current transient simulations with drift-diffusion simulations is discussed in Sec. S1 A in Supplemental Material [40].

B. Approximation of the ac solution

Now that we have found an approximation of the dc potential and net charge density, we can focus on solving the device capacitance. We aim to approximate the high-frequency capacitance as a function of time after application of a voltage pulse (capacitance transients) and the capacitance at 0 V at different frequencies (capacitance-frequency measurements). To compute the capacitance, we choose the sinusoidal steady state analysis, first introduced by Laux [41] and previously applied to organic and inorganic semiconductors [45–47]. This method is based on linearizing the Poisson equation and the electron and hole current continuity equations around a dc operating point. To simplify the derivation, we first express the non-time-dependent terms in the Poisson and current continuity equations in terms of F_Φ, F_n, and F_p:

$$F_\Phi(\Phi, n, p) = \frac{\epsilon}{e}\frac{d^2\Phi}{dx^2} + (p - n) = 0, \tag{11}$$

$$F_n(\Phi, n, t) - \frac{dn}{dt} = \frac{1}{e}\frac{dj_n}{dx} - r_n - \frac{dn}{dt} = 0, \tag{12}$$

$$F_p(\Phi, n, t) - \frac{dp}{dt} = -\frac{1}{e}\frac{dj_p}{dx} - r_p - \frac{dp}{dt} = 0, \tag{13}$$

where j_n and j_p are the electron and hole current densities, and r_n and r_p represent the electron and hole recombination. Because the techniques we focus on are performed in the dark, we can assume that r_n and r_p are negligible. We then extend the electron and hole densities and the potential into a dc term and an ac term:

$$\Phi = \Phi^{\mathrm{dc}} + \Phi^{\mathrm{ac}}e^{i\omega t}, \tag{14}$$

$$n = n^{\mathrm{dc}} + n^{\mathrm{ac}}e^{i\omega t}, \tag{15}$$

$$p = p^{\mathrm{dc}} + p^{\mathrm{ac}}e^{i\omega t}, \tag{16}$$

where i is the imaginary unit, and $\omega = 2\pi f$ is the angular perturbation frequency. After linearizing the Poisson and current continuity equations, we arrive at a system of equations:

$$\begin{bmatrix} \frac{dF_\Phi}{d\Phi} & \frac{dF_\Phi}{dn} & \frac{dF_\Phi}{dp} \\ \frac{dF_n}{d\Phi} & \frac{dF_n}{dn} - i\omega & \frac{dF_n}{dp} \\ \frac{dF_p}{d\Phi} & \frac{dF_p}{dn} & \frac{dF_p}{dp} - i\omega \end{bmatrix} \cdot \begin{bmatrix} \Phi^{\mathrm{ac}} \\ n^{\mathrm{ac}} \\ p^{\mathrm{ac}} \end{bmatrix} = 0, \tag{17}$$

which we can solve numerically for the position-dependent ac potential Φ^{ac}, ac electron density n^{ac}, and ac hole density p^{ac}. We can add a time dependency by solving Eq. (17) for the dc potentials and carrier densities during the transient. A detailed explanation of this derivation and the discretization of the semiconductor equations following Ref. [48] is given in Sec. S1 B in Supplemental Material [40]. In the case of capacitance transient simulations, we do not account for the contribution of ions to the small signal solution. We can make this simplification because the perturbation frequency is high. Thus, the contribution due to ionic polarization to the alternating current can be disregarded. When simulating capacitance-frequency measurements, we take mobile ions into account when computing the ac solution, as mobile ions dominate the ac solution at low frequencies. A comparison of capacitance transient and capacitance-frequency measurements with drift-diffusion simulations is given in Sec. S1 B in Supplemental Material [40].

C. Validation of the step model

We can now approximate the three measurement techniques: capacitance transient, current transient, and capacitance-frequency measurements. For the capacitance transient and current transient approximation, we solve the dc solution after application of a voltage pulse. The current density then follows from Eq. (10). For the capacitance transients, we solve the ac solution at each point in time at a perturbation frequency that is high enough so we can assume that no mobile ions contribute to the capacitance, in this case 20 kHz. For the capacitance-frequency technique, we solve the ac solution at 0 V dc bias and various frequencies. When directly comparing the step model with drift-diffusion simulations, as illustrated in Figs. S7, S10, and S11 in Supplemental Material [40], we generally observe only a slight offset between the step model and the drift-diffusion simulations. This difference illustrates that these techniques are sensitive to the minor differences in the dc solution between the step model and the drift-diffusion solution.

To validate the step model developed, we, therefore, choose to fit data generated with drift-diffusion simulations. We use the parameter set in Table S1 in Supplemental Material [40] for the drift-diffusion simulations and the step model. We simulate transients with voltage pulses of 0.8, 0.9, 1.0, and 1.1 V with drift-diffusion simulations and use the step model to fit the free parameters. We are

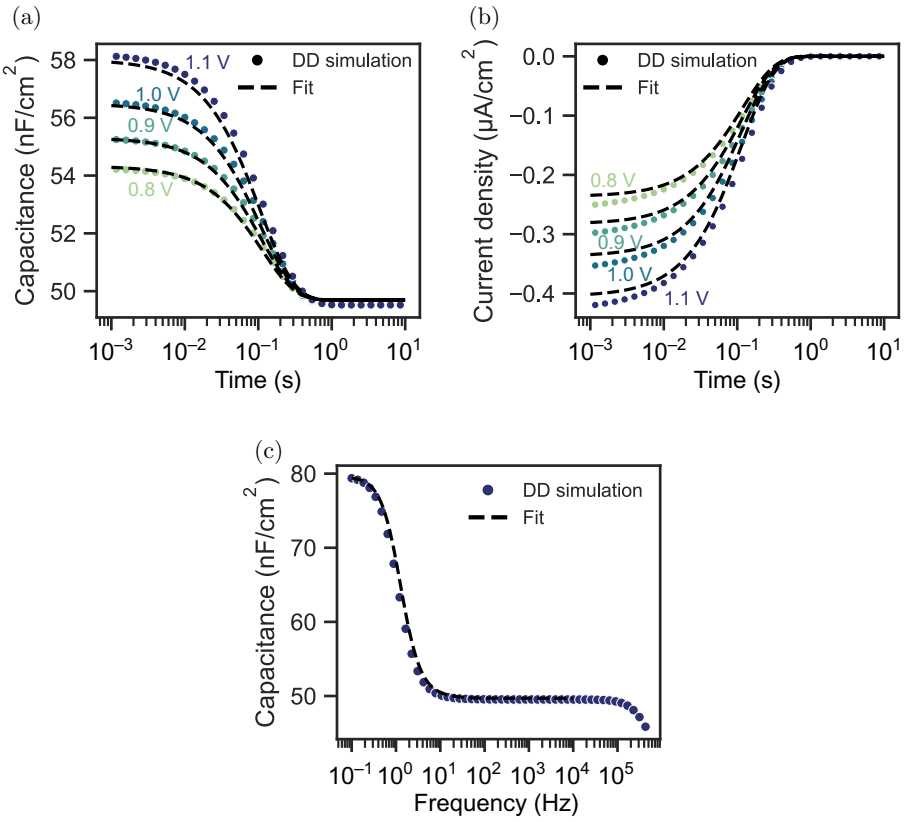

FIG. 3. Drift-diffusion (DD) simulations of (a) capacitance transient, (b) current transient, and (c) capacitance-frequency measurements. The dashed lines are fits with the step model. The ion density set in the drift-diffusion simulations is 10^{17} cm^{-3}. The fitted ion density and diffusion coefficient are listed in Table I.

interested mainly in determining the density and diffusion coefficient of the mobile ions. However, to account for the offset between the step model and the drift-diffusion simulations, we need to add additional fitting parameters. Here we choose to also fit the doping density of the ETL N_{ETL} and the dielectric constant of the perovskite $\epsilon_{\mathrm{r,pero}}$. Figure 3 shows results for the three different techniques for an ion density of 10^{17} cm^{-3} and an ionic diffusion coefficient of 9.1×10^{-11} cm^2/s at 300 K fitted with the step model. The extracted ion density is 1.1×10^{17} cm^{-3}, which is in good agreement with the density set in the drift-diffusion simulations. The extracted diffusion coefficient of 1.0×10^{-10} cm^2/s also matches the diffusion coefficient set in the drift-diffusion simulations well.

To test the limitations of the step model, we then fit a range of ion densities between 5×10^{16} and 5×10^{18} cm^{-3}, which are shown in Fig. S2 in Supplemental Material [40]. The extracted ion densities, diffusion coefficients, and ionic conductivities are listed in Table I. Ion densities below 5×10^{17} cm^{-3} can be determined accurately. For ion densities of 5×10^{17} and higher, the drift-diffusion simulations can be fitted with a range of ion densities and diffusion coefficients. This occurs when a significant fraction of the perovskite bulk is screened by mobile ions. Then, ion densities cannot be determined anymore [49]. This is illustrated in Fig. S13 in Supplemental Material [40], where we compare the fit residual of the drift-diffusion simulations with ion densities of 10^{17} and 10^{18} cm^{-3}. For an ion density of 10^{17} cm^{-3}, the fit in Fig. S13(a) converges to one ion density and diffusion coefficient. In contrast, for an ion density of 10^{18} cm^{-3}, the fit converges to a product of ion density and diffusion coefficient, which is proportional to the ionic conductivity [see Fig. S13(b)]. This limitation is further illustrated in Fig. S13(c), where a clear minimum for a set ion density of 10^{17} cm^{-3} is visible. In contrast, for a set ion density of 10^{18} cm^{-3}, the residual decreases as the ion density increases and does not show a significant difference for ion densities of 5×10^{17} cm^{-3} and higher. The step model also allows the easy computation of the fraction of the bulk where the electric field is zero, i.e., the electric field is screened. Figure S14 in Supplemental Material [40] shows this fraction for different ion densities. As can be seen, for ion densities of around 3×10^{17} cm^{-3} and higher, more than 90 % of the perovskite bulk is screened. This shows that simply checking if a significant fraction of the bulk is screened for a given ion density is a good way to verify extracted ion densities. Even though we cannot determine the ion

TABLE I. Ion densities N_{ion}, diffusion coefficients $D_{ion,300\,K}$, and ionic conductivities $\sigma_{ion,300\,K}$ when drift-diffusion simulations are fitted with the step model. For ion densities of 5×10^{17} cm^{-3} and higher, only the ionic conductivity can be determined.

N_{ion} (cm^{-3})		$D_{ion,300\,K}$ (cm^2/s)		$\sigma_{ion,300\,K}$ (S/cm)	
Set	Fit	Set	Fit	Set	Fit
5.0×10^{16}	5.8×10^{16}	9.1×10^{-11}	1.2×10^{-10}	2.8×10^{-11}	4.3×10^{-11}
1.0×10^{17}	1.1×10^{17}	9.1×10^{-11}	1.0×10^{-10}	5.7×10^{-11}	7.1×10^{-11}
5.0×10^{17}	...	9.1×10^{-11}	...	2.8×10^{-10}	3.1×10^{-10}
1.0×10^{18}	...	9.1×10^{-11}	...	5.7×10^{-10}	6.5×10^{-10}
5.0×10^{18}	...	9.1×10^{-11}	...	2.8×10^{-9}	3.1×10^{-9}

density, we can still accurately estimate the ionic conductivity, which is listed in Table I. We additionally fit temperature-activated capacitance transients, current transients, and capacitance-frequency measurements, shown in Fig. S15 in Supplemental Material [40]. With the step model developed, we can accurately predict the activation energy of 0.3 eV, set in the drift-diffusion simulations.

D. Application of the step model to a measured device

We now apply the step model to quantify the properties of mobile ions in an experimental realization of a perovskite solar cell in the configuration indium tin oxide/(2-(3,6-Dimethoxy-9H-carbazol-9-yl)ethyl)phosphonic acid (Meo-2PACz)/cesium-methylammonium-formamidinium $Cs_{0.05}(MA_{0.05}FA_{0.95})_{0.95}$ $Pb(I_{0.95}Br_{0.05})3/C_{60}$/bathocuproine/Cu [50]. An exemplary current density vs voltage measurement is shown in Fig. S16 in Supplemental Material [40]. We performed capacitance transient, current transient, and capacitance-frequency measurements at different temperatures; see Fig. S17 in Supplemental Material [40]. Details about the fabrication process and the characterization are described in Sec. S3 in Supplemental Material [40]. With increasing temperature, the capacitance transient measurements in Fig. S17(a) shift to shorter times, while the capacitance in Fig. S17(c) shifts to higher frequencies. This trend is in line with a temperature-activated ionic conductivity. Interestingly, we observe a decrease of the initial current amplitude in the current transient measurements in Fig. S17(b) for temperatures

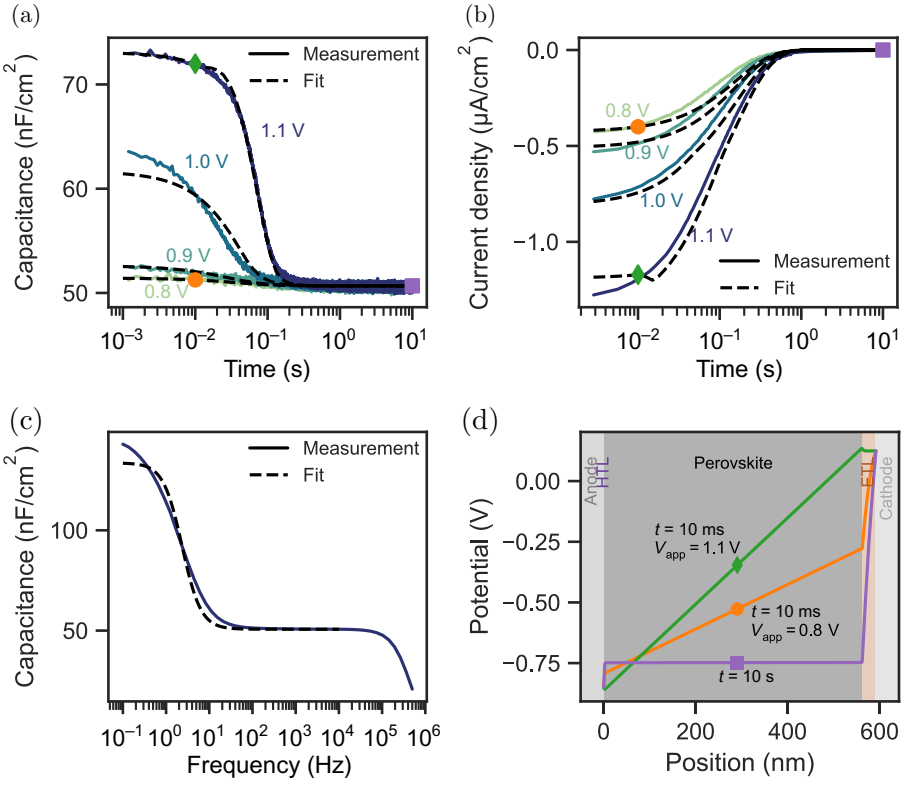

FIG. 4. (a) Capacitance transient, (b) current transient, and (c) capacitance-frequency measurements of a perovskite solar cell. The dashed lines are fits with the step model. (d) Approximated potential at 0 V, 10 ms and 10 s after the voltage pulses of 0.8 V or 1.1 V are removed. The markers link the potential distributions to the capacitance and current transient plots.

TABLE II. Average values for the ionic conductivity at 260 and 300 K and the activation energy of the diffusion coefficient $E_{a,ion}$ extracted from fitting capacitance transient $C(t)$, current transient[$J(t)$, and capacitance-frequency $C(f)$ measurements. The values are the average values and standard deviations from fitting three different devices.

Technique	$\sigma_{ion,260\,K}$ (S/cm)	$\sigma_{ion,300\,K}$ (S/cm)	$E_{a,ion}$ (eV)
$C(t)$	$(1.0 \pm 0.4) \times 10^{-10}$	$(4.0 \pm 1.6) \times 10^{-10}$	0.25 ± 0.01
$J(t)$	$(0.7 \pm 0.2) \times 10^{-10}$	...	...
$C(f)$	$(2.0\pm)0.8 \times 10^{-10}$	$(1.4 \pm 0.3) \times 10^{-9}$	0.36 ± 0.03

greater than 280 K. However, we expect the current amplitude to increase with increasing temperature due to the higher ionic conductivity, as illustrated in the temperature-dependent current transient simulations in Fig. S15. Possibly, the current transient measurements at higher temperatures are impacted by additional temperature-activated processes influencing, for example, the charge transport layers [20] or creating additional ions [35]. The unexpected temperature dependency of the current transients illustrates the complexity of their interpretation. The precise origin of the decrease in the current amplitude is beyond the scope of this work. We therefore focus on the regime between 260 and 280 K, the region where we observe the expected behavior of an increasing current amplitude. The measurements at 260 K are shown in Fig. 4. Because we do not know the initial distribution of the mobile ions, we measure the capacitance and current transients at different voltage pulses from 0.8 to 1.1 V. In the capacitance transient measurements in Fig. 4(a), the capacitance remains almost unchanged for voltages of 0.8 and 0.9 V. Then, at 1.0 and 1.1 V the initial capacitance increases significantly. Also, in the current transient measurements in Fig. 4(b), we observe an increase in the current amplitude with applied voltage. The capacitance-frequency measurements in Fig. 4(c) show the expected increase of the capacitance at low frequencies due to ionic polarization [20,39]. To unravel the device parameters and ionic properties, we fit the measurements with the step model developed . The device parameters used in the step model are listed in Table S2. We assume that the ETL is moderately doped. If that were not the case, most of the potential would drop in the ETL, and there would be almost no accumulation of ions at the HTL/perovskite interface. This situation would lead to little change in the amplitude of the capacitance transient measurements and only a small increase in the low-frequency capacitance in the capacitance-frequency measurements. For many device parameters, including the doping density of the ETL, the conduction band offset of the ETL, the work function of the anode, and the dielectric constants of the different layers, we can only estimate a range. We, therefore, start by globally fitting the capacitance transient and capacitance-frequency measurements to estimate these parameters. The results are listed in Table S3 in Supplemental Material [40]. We can estimate the built-in potential of the device (the difference between the work function of the anode and the conduction band of the doped ETL), an often unknown parameter, to be around 1.0 V. We then individually fit the different measurements, focusing only on the ionic parameters, which are illustrated as dashed lines in Fig. 4 and show good agreement with the measurements. As a result, we get insight into the approximated potential and net charge density [see Fig. 4(d)] and can explain the origin of the increasing amplitude in the capacitance transient and current transient measurements. The increase of the capacitance at voltages of 1.0 and 1.1 V is due to mobile ions that accumulate at the perovskite/ETL interface during the voltage pulses. Simultaneously, mobile ions are depleted from the HTL/perovskite interfaces. The ions accumulated at the perovskite/ETL interface are then screened by electrons at the interface [evident in the flat and slightly increasing potential for $V_{app} = 1.1$ V and $t = 10$ ms at the perovskite/ETL interface in Fig. 4(d)]. The accumulation of electronic charges then leads to the larger initial capacitance. In contrast, for a voltage pulse of 0.8 V, the ETL is already depleted at 10 ms [see Fig. 4(d)], explaining the low value of the initial capacitance. The increased accumulation of ions at the ETL interface with increasing voltage also leads to a higher bulk electric field [higher slope of the potential in Fig. 4(d)], explaining the increased amplitude in the current transient measurements. We note that the shoulder at short times in the 1.1 V current transients originates from a slight discontinuity in the electric field solution when switching from the reverse accumulation case (ions accumulated at the ETL interface) to the normal accumulation case (ions accumulated at the HTL interface).

Regarding the ionic parameters, we cannot determine the ion density, because a significant fraction of the perovskite is screened, as can be seen in Fig. 4(d). This results in no clear minimum of the residual (see Fig. S18 in Supplemental Material [40]). Therefore, we can only extract the ionic conductivity from electronic measurements. At 260 K, the extracted ionic conductivities show good agreement between the techniques, with ionic conductivities of 1.0×10^{-10} S/cm for capacitance transient measurements, 0.7×10^{-10} S/cm for current transient measurements, and 2.0×10^{-10} S/cm for capacitance-frequency measurements (see Table II). The characteristic times of the different measurements also allow estimation of the scan rate at which the ion-induced loss would result in significant hysteresis.

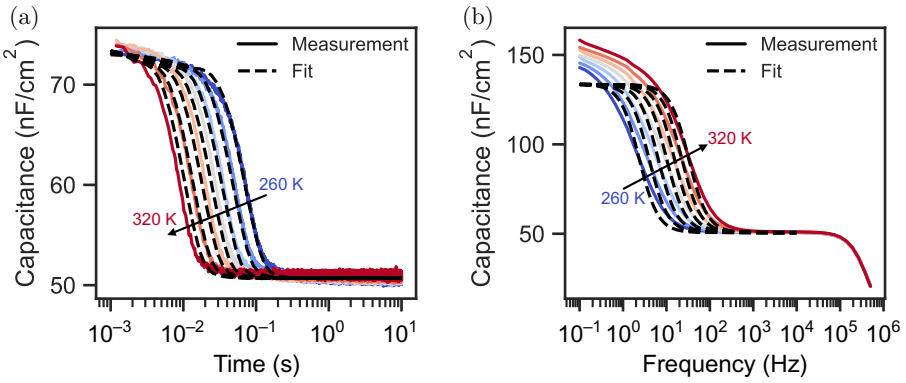

FIG. 5. (a) Capacitance transient and (b) capacitance-frequency measurements at temperatures from 260 to 320 K in steps of 10 K. The dashed lines are fits with the step model.

Lastly, we determine the activation energy on the basis of the capacitance transient and capacitance-frequency measurements at different temperatures. We do not extract the activation energy from the current transient measurements because we cannot capture the decreased current amplitude at higher temperatures with the step model. Assuming a temperature-activated ionic diffusion coefficient [51,52]

$$D_{\text{ion}} = D_0 e^{-\frac{E_{\text{a,ion}}}{k_B T}}, \tag{18}$$

with prefactor D_0 and activation energy $E_{\text{a,ion}}$, we fit the capacitance transient and capacitance-frequency measurements, as Fig. 5 illustrates. We extract an activation energy of 0.25 eV for the capacitance transient measurements and an activation energy of 0.36 eV for the capacitance-frequency measurements. We attribute the discrepancy between the activation energies to the difference in the operation point of the techniques. In transient techniques, we apply a bias before the measurement during which we possibly activate mobile ions. In contrast, the capacitance-frequency measurements are performed at 0 V dc bias. Additionally, the capacitance and current transient measurements are mainly sensitive to the perovskite bulk, whereas the capacitance-frequency measurements mainly probe the interface between the perovskite and the CTLs. Local differences between the bulk and the interfaces can, therefore, result in differences between the extracted properties of the mobile ions. Finally, we calculate the ionic conductivities at 300 K, which are listed in Table II. For the capacitance transient measurements, we extract an ionic conductivity of 4.0×10^{-10} S/cm. For the capacitance-frequency measurements, we get a value of 1.4×10^{-9} S/cm. These values lie in a typical range of ionic conductivities observed in perovskite solar cells [12,53].

III. CONCLUSION

In this work, we have developed an approach to characterize mobile ions based on capacitance transient, current transient, and capacitance-frequency measurements. The approach is based on approximating drift-diffusion simulations with a computationally inexpensive model. Expressing the net charge density of ionic accumulation and depletion layers and, crucially, the depletion layers in the CTLs leads to an accurate approximation of the dc potential. After introducing a time dependency in the dc solution and calculating the ac solution on the basis of the sinusoidal steady-state analysis, we could approximate capacitance transient, current transient, and capacitance-frequency measurements. We then validated the step model by extracting ionic parameters from drift-diffusion simulations. Within the accessible regime, we could accurately determine the ion densities and diffusion coefficients. Above an upper threshold where electrical measurements do not allow an accurate estimation of ion densities, we could still accurately determine the ionic conductivity. Lastly, we applied the step model to characterize perovskite solar cells. We fit the results obtained with three measurement techniques, capacitance transient, current transient, and capacitance-frequency measurements, with the step model, resulting in valuable information about device parameters such as the built-in potential, which we determined to be around 1.0 V. With the step model, we could then extract an ionic conductivity between 4.0×10^{-10} and 1.4×10^{-9} S/cm and an activation energy between 0.25 and 0.36 eV.

Overall, the balance between the simplicity and accuracy of the step model developed allows an accurate characterization of mobile ionic carriers in perovskite solar cells. Furthermore, in combination with the simplicity of electrical measurements, the step model offers a powerful tool to study ion migration in perovskite solar cells and is openly accessible [30].

ACKNOWLEDGMENTS

The authors thank Lars Sonneveld, Francesco Le Pera, and Larissa van de Ven for testing the code. The work

of M.C.S., A.O.A., J.J.d.B., and B.E. received funding from the European Research Council under the European Union's Horizon 2020 research and innovation program under Grant Agreement No. 947221. The work was performed at the NWO-I institute AMOLF as part of the research program of the Dutch Research Council and was performed at the research institute AMOLF. B.A.S and F.L. received funding from the Volkswagen Foundation via the Freigeist program.

M.C.S conceived the work, derived the step model, performed the simulations and electrical measurements, performed the analysis, interpreted the results, and wrote the manuscript. A.O.A. helped with the derivation and commented on the manuscript. B.A.S. fabricated the perovskite solar cells and commented on the manuscript. J.J.d.B. performed thin-film thickness measurements. F.L. commented on the manuscript and supervised B.A.S. B.E conceived and supervised the work, interpreted the results, and edited the manuscript.

DATA AVAILABILITY

The data that support the findings of this article are openly available [54].

[1] M. A. Green, E. D. Dunlop, M. Yoshita, N. Kopidakis, K. Bothe, G. Siefer, D. Hinken, M. Rauer, J. Hohl-Ebinger, and X. Hao, Solar cell efficiency tables (version 64), Prog. Photovolt.: Res. Appl. **32**, 425 (2024).

[2] National Renewable Energy Laboratory, Best research-cell efficiency chart, https://www2.nrel.gov/pv/cell-efficiency (accessed: 2025-04-15).

[3] Z. Shen, Q. Han, X. Luo, Y. Shen, Y. Wang, Y. Yuan, Y. Zhang, Y. Yang, and L. Han, Efficient and stable perovskite solar cells with regulated depletion region, Nat. Photonics **18**, 450 (2024).

[4] Y. Yang, H. Chen, C. Liu, J. Xu, C. Huang, C. D. Malliakas, H. Wan, A. S. R. Bati, Z. Wang, R. P. Reynolds, I. W. Gilley, S. Kitade, T. E. Wiggins, S. Zeiske, S. Suragtkhuu, M. Batmunkh, L. X. Chen, B. Chen, M. G. Kanatzidis, and E. H. Sargent, Amidination of ligands for chemical and field-effect passivation stabilizes perovskite solar cells, Science **386**, 898 (2024).

[5] Y. Zhao, W. Zhou, H. Tan, R. Fu, Q. Li, F. Lin, D. Yu, G. Walters, E. H. Sargent, and Q. Zhao, Mobile-ion-induced degradation of organic hole-selective layers in perovskite solar cells, J. Phys. Chem. C **121**, 14517 (2017).

[6] E. T. Hoke, D. J. Slotcavage, E. R. Dohner, A. R. Bowring, H. I. Karunadasa, and M. D. McGehee, Reversible photo-induced trap formation in mixed-halide hybrid perovskites for photovoltaics, Chem. Sci. **6**, 613 (2015).

[7] Z. Fang, T. Nie, S. F. Liu, and J. Ding, Overcoming phase segregation in wide-bandgap perovskites: From progress to perspective, Adv. Funct. Mater. **34**, 2404402 (2024).

[8] V. M. Le Corre, J. Diekmann, F. Peña-Camargo, J. Thiesbrummel, N. Tokmoldin, E. Gutierrez-Partida, K. P. Peters, L. Perdigón-Toro, M. H. Futscher, F. Lang, J. Warby, H. J. Snaith, D. Neher, and M. Stolterfoht, Quantification of efficiency losses due to mobile ions in perovskite solar cells via fast hysteresis measurements, Solar RRL **6**, 2100772 (2022).

[9] J. Thiesbrummel, *et al.*,Ion-induced field screening as a dominant factor in perovskite solar cell operational stability, Nat. Energy **9**, 664 (2024).

[10] S. Shah, *et al.*, Impact of ion migration on the performance and stability of perovskite-based tandem solar cells, Adv. Energy Mater. **14**, 2400720 (2024).

[11] J. Thiesbrummel, V. M. Le Corre, F. Peña-Camargo, L. Perdigón-Toro, F. Lang, F. Yang, M. Grischek, E. Gutierrez-Partida, J. Warby, M. D. Farrar, S. Mahesh, P. Caprioglio, S. Albrecht, D. Neher, H. J. Snaith, and M. Stolterfoht, Universal current losses in perovskite solar cells due to mobile ions, Adv. Energy Mater. **11**, 2101447 (2021).

[12] M. Diethelm, T. Lukas, J. Smith, A. Dasgupta, P. Caprioglio, M. Futscher, R. Hany, and H. J. Snaith, Probing ionic conductivity and electric field screening in perovskite solar cells: A novel exploration through ion drift currents, Energy Environ. Sci. **18**, 1385 (2025).

[13] A. O. Alvarez, M. García-Batlle, F. Lédée, E. Gros-Daillon, J. M. Guillén, J.-M. Verilhac, T. Lemercier, J. Zaccaro, L. F. Marsal, O. Almora, and G. Garcia-Belmonte, Ion migration and space-charge zones in metal halide perovskites through short-circuit transient current and numerical simulations, Adv. Electron. Mater. **10**, 2400241 (2024).

[14] C. Xu, M. S. Alvar, G.-J. A. H. Wetzelaer, and P. W. M. Blom, Analysis of the ionic and dielectric properties of perovskites by impedance spectroscopy, J. Appl. Phys. **133**, 045501 (2023).

[15] C. Messmer, J. Parion, C. V. Meza, S. Ramesh, M. Bivour, M. Heydarian, J. Schön, H. S. Radhakrishnan, M. C. Schubert, and S. W. Glunz, Understanding ion-related performance losses in perovskite-based solar cells by capacitance measurements and simulation, Solar RRL **8**, 2400630 (2024).

[16] M. C. Schmidt, A. O. Alvarez, J. J. De Boer, L. J. Van De Ven, and B. Ehrler, Consistent interpretation of time- and frequency-domain traces of ion migration in perovskite semiconductors, ACS Energy Lett. **9**, 5850 (2024).

[17] L. McGovern, G. Grimaldi, M. H. Futscher, E. M. Hutter, L. A. Muscarella, M. C. Schmidt, and B. Ehrler, Reduced barrier for ion migration in mixed-halide perovskites, ACS Appl. Energy Mater. **4**, 13431 (2021).

[18] M. H. Futscher, J. M. Lee, L. McGovern, L. A. Muscarella, T. Wang, M. I. Haider, A. Fakharuddin, L. Schmidt-Mende, and B. Ehrler, Quantification of ion migration in $CH_3NH_3PbI_3$ perovskite solar cells by transient capacitance measurements, Mater. Horiz. **6**, 1497 (2019).

[19] S. Ravishankar, Z. Liu, U. Rau, and T. Kirchartz, Multilayer capacitances: How selective contacts affect capacitance measurements of perovskite solar cells, PRX Energy **1**, 013003 (2022).

[20] R. A. Awni, Z. Song, C. Chen, C. Li, C. Wang, M. A. Razooqi, L. Chen, X. Wang, R. J. Ellingson, J. V. Li, and Y. Yan, Influence of charge transport layers on capacitance measured in halide perovskite solar cells, Joule **4**, 644 (2020).

[21] M. C. Schmidt, E. Gutierrez-Partida, M. Stolterfoht, and B. Ehrler, Impact of mobile ions on transient capacitance measurements of perovskite solar cells, PRX Energy **2**, 043011 (2023).
[22] V. M. Le Corre, M. Stolterfoht, L. Perdigón Toro, M. Feuerstein, C. Wolff, L. Gil-Escrig, H. J. Bolink, D. Neher, and L. J. A. Koster, Charge transport layers limiting the efficiency of perovskite solar cells: How to optimize conductivity, doping, and thickness, ACS Appl. Energy Mater. **2**, 6280 (2019).
[23] E. A. Duijnstee, J. M. Ball, V. M. Le Corre, L. J. A. Koster, H. J. Snaith, and J. Lim, Toward understanding space-charge limited current measurements on metal halide perovskites, ACS Energy Lett. **5**, 376 (2020).
[24] N. Tessler and Y. Vaynzof, Insights from device modeling of perovskite solar cells, ACS Energy Lett. **5**, 1260 (2020).
[25] S. Bitton and N. Tessler, Perovskite ionics—Elucidating degradation mechanisms in perovskite solar cells *via* device modelling and iodine chemistry, Energy Environ. Sci. **16**, 2621 (2023).
[26] N. E. Courtier, J. M. Foster, S. E. J. O'Kane, A. B. Walker, and G. Richardson, Systematic derivation of a surface polarisation model for planar perovskite solar cells, Eur. J. Appl. Math. **30**, 427 (2019).
[27] N. E. Courtier, J. M. Cave, J. M. Foster, A. B. Walker, and G. Richardson, How transport layer properties affect perovskite solar cell performance: Insights from a coupled charge transport/ion migration model, Energy Environ. Sci. **12**, 396 (2019).
[28] L. Bertoluzzi, C. C. Boyd, N. Rolston, J. Xu, R. Prasanna, B. C. O'Regan, and M. D. McGehee, Mobile ion concentration measurement and open-access band diagram simulation platform for halide perovskite solar cells, Joule **4**, 109 (2020).
[29] Setfos simulation software, https://www.fluxim.com/setfos-intro (accessed: 2025-07-20).
[30] M. Schmidt, Code to approximate drift-diffusion simulation, https://github.com/AMOLF-Hybrid-Solar-Cells/DD-Approximation_CtJtCf (2025).
[31] S. G. McCallum, O. Nicholls, K. O. Jensen, M. V. Cowley, J. E. Lerpinière, and A. B. Walker, Bayesian parameter estimation for characterising mobile ion vacancies in perovskite solar cells, J. Phys.: Energy **6**, 015005 (2024).
[32] G. Richardson, S. E. J. O'Kane, R. G. Niemann, T. A. Peltola, J. M. Foster, P. J. Cameron, and A. B. Walker, Can slow-moving ions explain hysteresis in the current–voltage curves of perovskite solar cells? Energy Environ. Sci. **9**, 1476 (2016).
[33] C. Eames, J. M. Frost, P. R. F. Barnes, B. C. O'Regan, A. Walsh, and M. S. Islam, Ionic transport in hybrid lead iodide perovskite solar cells, Nat. Commun. **6**, 7497 (2015).
[34] J. Haruyama, K. Sodeyama, L. Han, and Y. Tateyama, First-principles study of ion diffusion in perovskite solar cell sensitizers, J. Am. Chem. Soc. **137**, 10048 (2015).
[35] J. M. Azpiroz, E. Mosconi, J. Bisquert, and F. De Angelis, Defect migration in methylammonium lead iodide and its role in perovskite solar cell operation, Energy Environ. Sci. **8**, 2118 (2015).
[36] A. Walsh, D. O. Scanlon, S. Chen, X. G. Gong, and S.-H. Wei, Self-regulation mechanism for charged point defects in hybrid halide perovskites, Angew. Chem., Int. Ed. **54**, 1791 (2015).
[37] E. Mosconi and F. De Angelis, Mobile ions in organohalide perovskites: Interplay of electronic structure and dynamics, ACS Energy Lett. **1**, 182 (2016).
[38] F. Peña-Camargo, J. Thiesbrummel, H. Hempel, A. Musienko, V. M. Le Corre, J. Diekmann, J. Warby, T. Unold, F. Lang, D. Neher, and M. Stolterfoht, Revealing the doping density in perovskite solar cells and its impact on device performance, Appl. Phys. Rev. **9**, 021409 (2022).
[39] O. Almora, I. Zarazua, E. Mas-Marza, I. Mora-Sero, J. Bisquert, and G. Garcia-Belmonte, Capacitive dark currents, hysteresis, and electrode polarization in lead halide perovskite solar cells, J. Phys. Chem. Lett. **6**, 1645 (2015).
[40] See Supplemental Material at http://link.aps.org/supplemental/10.1103/mr3l-jg9h for the derivation of the approximation, parameters of the drift-diffusion simulations, fits of the drift-diffusion simulations, a description of the device fabrication and electrical characterization, and fit residuals of the measurements. References [21,28,32,41,43,48,50,55–57] are cited in Supplemental Material.
[41] S. Laux, Techniques for small-signal analysis of semiconductor devices, IEEE Trans. Comput.-Aided Des. Integr. Circuits Syst. **4**, 472 (1985).
[42] S. M. Sze and K. K. Ng, *Physics of Semiconductor Devices* (Wiley-Interscience, Hoboken, NJ, 2007), 3rd ed.
[43] S. E. J. O'Kane, G. Richardson, A. Pockett, R. G. Niemann, J. M. Cave, N. Sakai, G. E. Eperon, H. J. Snaith, J. M. Foster, P. J. Cameron, and A. B. Walker, Measurement and modelling of dark current decay transients in perovskite solar cells, J. Mater. Chem. C **5**, 452 (2017).
[44] M. Pitaro, E. K. Tekelenburg, S. Shao, and M. A. Loi, Tin halide perovskites: From fundamental properties to solar cells, Adv. Mater. **34**, 2105844 (2022).
[45] E. Knapp and B. Ruhstaller, Numerical impedance analysis for organic semiconductors with exponential distribution of localized states, Appl. Phys. Lett. **99**, 093304 (2011).
[46] Q. Li and R. Dutton, Numerical small-signal AC modeling of deep-level-trap related frequency-dependent output conductance and capacitance for GaAs MESFET's on semi-insulating substrates, IEEE Trans. Electron Dev. **38**, 1285 (1991).
[47] M. Gaitan and I. D. Mayergoyz, A numerical analysis for the small-signal response of the MOS capacitor, Solid State Electron. **32**, 207 (1989).
[48] S. Selberherr, *Analysis and Simulation of Semiconductor Devices* (Springer Vienna, Vienna, 1984).
[49] M. C. Schmidt and B. Ehrler, How many mobile ions can electrical measurements detect in perovskite solar cells? ACS Energy Lett. **10**, 2457 (2025).
[50] B. A. Seid, S. Sarisozen, F. Peña-Camargo, S. Ozen, E. Gutierrez-Partida, E. Solano, J. A. Steele, M. Stolterfoht, D. Neher, and F. Lang, Understanding and mitigating atomic oxygen-induced degradation of perovskite solar cells for near-Earth space applications, Small **20**, 2311097 (2024).
[51] S. Reichert, Q. An, Y.-W. Woo, A. Walsh, Y. Vaynzof, and C. Deibel, Probing the ionic defect landscape in halide perovskite solar cells, Nat. Commun. **11**, 6098 (2020).
[52] W. Zhu, S. Wang, X. Zhang, A. Wang, C. Wu, and F. Hao, Ion migration in organic–inorganic hybrid perovskite solar

cells: Current understanding and perspectives, Small **18**, 2105783 (2022).

[53] T.-Y. Yang, G. Gregori, N. Pellet, M. Grätzel, and J. Maier, The significance of ion conduction in a hybrid organic–inorganic lead-iodide-based perovskite photosensitizer, Angew. Chem., Int. Ed. **54**, 7905 (2015).

[54] M. C. Schmidt, A. O. Alvarez, B. A. Seid, J. J. de Boer, F. Lang, and B. Ehrler, Experimental and simulation datasets, https://doi.org/10.5281/zenodo.16890531.

[55] N. E. Courtier, J. M. Cave, A. B. Walker, G. Richardson, and J. M. Foster, IonMonger: A free and fast planar perovskite solar cell simulator with coupled ion vacancy and charge carrier dynamics, J. Comput. Electron. **18**, 1435 (2019).

[56] M. Stolterfoht, P. Caprioglio, C. M. Wolff, J. A. Márquez, J. Nordmann, S. Zhang, D. Rothhardt, U. Hörmann, Y. Amir, A. Redinger, L. Kegelmann, F. Zu, S. Albrecht, N. Koch, T. Kirchartz, M. Saliba, T. Unold, and D. Neher, The impact of energy alignment and interfacial recombination on the internal and external open-circuit voltage of perovskite solar cells, Energy Environ. Sci. **12**, 2778 (2019).

[57] G. B. Alers, B. Golding, A. R. Kortan, R. C. Haddon, and F. A. Theil, Existence of an orientational electric dipolar response in C_{60} single crystals, Science **257**, 511 (1992).